

# Aerodynamic Shape Optimization for Natural Laminar Flow Using a Discrete-Adjoint Approach

Ramy Rashad\* and David W. Zingg†

*University of Toronto, Toronto, Ontario M3H 5T6, Canada*

The design of natural-laminar-flow airfoils is demonstrated by high-fidelity, multipoint, aerodynamic shape optimization capable of efficiently incorporating and exploiting laminar-turbulent transition. First, a two-dimensional Reynolds-averaged Navier-Stokes (RANS) flow solver has been extended to incorporate an iterative laminar-turbulent transition prediction methodology. The natural transition locations due to Tollmien-Schlichting instabilities are predicted using the simplified  $e^N$  envelope method of Drela and Giles or alternatively, the compressible form of the Arnal-Habiballah-Delcourt criterion. The boundary-layer properties are obtained directly from the Navier-Stokes flow solution, and the transition to turbulent flow is modeled using an intermittency function in conjunction with the Spalart-Allmaras turbulence model. The RANS solver is subsequently employed in a gradient-based sequential quadratic programming shape optimization framework. The laminar-turbulent transition criteria are tightly coupled into the objective and gradient evaluations. The gradients are obtained using a new augmented discrete-adjoint formulation for non-local transition criteria. The aerodynamic design requirements are cast into a multipoint design optimization problem. A composite objective is defined using a weighted integral of the operating points. A Pareto front is also formed to study and quantify off-design performance. The proposed framework is applied to the single and multipoint optimization of subsonic and transonic airfoils, leading to robust natural-laminar-flow designs.

## I. Introduction and Motivation

THE current push for environmentally responsible aviation requires serious efforts to mitigate the escalating effects of such technology on climate change and natural resources. A clear vision for the efficiency of future transport aircraft – with specific targets for reduced fuel burn, emissions and noise – has been published in the U.S. National Aeronautics Research and Development Plan.<sup>1</sup> As a result, manufacturers and researchers are investigating both conventional and unconventional aircraft designs to meet these targets. As part of the effort to reduce fuel burn and emissions, aerodynamicists are assessing the feasibility of natural laminar flow (NLF) as a key enabler of environmentally responsible commercial aviation.

In the late nineteenth and early twentieth centuries, the breakthrough work of Reynolds and Prandtl began to shed light on boundary layers and laminar-turbulent transition.<sup>2</sup> More than a century has passed, and designers have become heavily reliant on Computational Fluid Dynamics (CFD), as well as single and multidisciplinary design optimization tools. Despite this, there remain few NLF applications in the current commercial fleet, with Honda's recent HA-420 business jet<sup>3</sup> and the nacelles on the recent Boeing 787<sup>4</sup> being among the first, if not the only applications to date. Over the past few decades, the use of CFD under the assumption of fully-turbulent conditions has allowed for significant advancements in aerodynamic design, but the conservatism leaves something to be desired. Indeed, design tools capable of incorporating and exploiting laminar-turbulent transition enable the design of aircraft with significantly reduced drag.

The lack of NLF applications in the fleet points to the sparsity of available design tools for NLF; it also points to the challenges in reliably realizing extended regions of laminar flow in flight. The transition to

\*PhD Candidate and AIAA Student Member

†Professor and Director, J. Armand Bombardier Foundation Chair in Aerospace Flight, AIAA Associate Fellow

turbulence is affected by many factors, including: Reynolds number ( $Re$ ), freestream turbulence intensity ( $T_u$ ), pressure gradient, Mach number ( $M$ ), surface roughness and heating, structural noise, rain, hail, icing, and insect impacts.<sup>2,4,5,6</sup>

Although the preceding list of factors is quite formidable, so are the economic and environmental incentives to investigate the theoretical, experimental, and computational methods that may actualize NLF in commercial aviation. Hence, engineers are exploring a variety of techniques that work to promote laminar flow, including: shaping the aircraft to maintain favourable pressure gradients and with lower sweep angles to reduce cross-flow instabilities, distributing surface roughness elements to stabilize crossflow instabilities, slat-less wing configurations, boundary-layer suction and wall heating, plasma and piezoelectric actuators, non-stick materials and coatings, and new manufacturing and maintenance procedures. Therefore, the development of design tools capable of efficiently exploiting any of the available techniques is of immediate consequence and benefit.

In this work, NLF design is demonstrated through high-fidelity, single and multipoint aerodynamic shape optimization with transition prediction capable of accounting for the effects of  $Re$ ,  $T_u$ ,  $M$ , and pressure gradient. The Reynolds-averaged Navier-Stokes (RANS) equations are solved with the one-equation Spalart-Allmaras (SA) turbulence model. The solver is first extended to incorporate an iterative laminar-turbulent transition prediction methodology and is subsequently employed in a gradient-based Sequential Quadratic Programming (SQP) shape optimization framework. Practical design requirements are cast into a parallelized multipoint design optimization problem. The proposed framework presents a good compromise between accuracy, robustness, and efficiency, resulting in a flexible and high-fidelity RANS-based optimization framework for NLF design in subsonic and transonic flight.

## II. Background

### II.A. Transition Prediction in RANS Solvers

The challenges in reliably predicting laminar-turbulent transition continue to limit our ability to compute many aerodynamic flows with accuracy.<sup>7</sup> Consequently, the development of transition prediction methods of varying complexity and fidelity is ongoing. While there are several mechanisms that may lead to transition, the two dominant mechanisms typically encountered in high-speed external aerodynamic flows are Tollmien-Schlichting and crossflow instabilities.<sup>8</sup>

The turbulence models used in RANS solvers do not have the stand-alone capability to predict the laminar-turbulent transition locations in a flow field; in order to predict transition, one must apply a transition criterion. In recent years, several approaches for incorporating transition prediction into RANS solvers have been developed. A review by Arnal *et al.*<sup>9</sup> discusses the various advantages and disadvantages of each approach in detail. The following list attempts to categorize the available strategies:

1. Coupling of a RANS code with a linear or parabolized stability solver and the  $e^N$  criterion.<sup>10,11,12,13,14</sup>
2. Direct implementation of simplified  $e^N$  methods into the RANS code.<sup>6,15,16,17</sup>
3. Direct implementation of analytical transition onset functions (criteria typically based on  $Re_x$  or  $Re_\theta$ ) into the RANS code.<sup>18,15,16,19</sup>
4. Coupling of a RANS code with a boundary-layer code and transition prediction using the criteria of methods 1 through 3 applied to the boundary-layer solution.<sup>11,20,21</sup>
5. Coupling of additional transport equations to the RANS turbulence model, such as the  $\gamma-Re_\theta$  transition model developed by Langtry and Menter.<sup>22,23,24,25,26</sup> These approaches make use of analytical transition onset functions built into the transport equations.

In the above strategies, the transition criteria employed by the RANS solvers are based on either the  $e^N$  criterion or on transition onset functions. To apply the  $e^N$  criterion one must first approximate the N-factor curves, representing the amplification ratios of the unstable frequencies of the disturbances in the boundary-layer. Transition is assumed to occur when the maximum local N-factor has exceeded some critical value ( $N_{crit}$ ). Values for  $N_{crit}$  must be specified *a priori* based on the freestream turbulence intensity and/or experimental calibration. In computing the N-factor curves, there are several methods of varying fidelity and computational cost. The highest fidelity approach (for RANS solvers) is to solve the parabolized or linearized stability equations at each station to obtain the local N-factors for the unstable frequencies.

Simplified approaches have been developed to alleviate the demanding computational cost of such methods, including: the use of database methods generated from linear stability studies, approximating the N-factor envelope through boundary-layer properties (such as the shape factor), and approximating the N-factor through the pressure gradient and curve fits based on linear stability theory, without the need for boundary-layer properties.<sup>4</sup>

Examples of transition criteria based on a transition onset function are Michel, Granville,  $H-Re_x$ , Abu-Ghannam and Shaw, Gleyzes-Habiballah, and Arnal-Habiballah-Delcourt.<sup>18,19,22</sup> These methods have been classified as “simpler” or “analytical” transition criteria.<sup>9</sup> Each have their range of applicability and limitations. These criteria typically compare the boundary-layer properties or related quantities (such as  $Re_\theta$ ) to an empirically calibrated transition onset function (such as  $Re_{\theta_{tr}}$ ). The transition onset functions are typically computed from the integrated boundary-layer properties; the exception being the local transport equation approach developed by Langtry and Menter.<sup>23</sup> The transition point is the first point at which, for example,  $Re_\theta \geq Re_{\theta_{tr}}$ .

In this work, for the prediction of the natural transition locations due to Tollmien-Schlichting instabilities, we employ approaches 2 and 3 from the above list. The boundary-layer properties are computed directly from the Navier-Stokes solution.<sup>27</sup> The framework makes use of Drela’s  $e^N$  envelope method<sup>28</sup> in approach 2, and the relatively new compressible form of the AHD criterion<sup>18</sup> in approach 3; these criteria are presented in Sections III.A and III.B, respectively. Transition prediction is implemented into the RANS solver using an iterative approach, and transition to turbulence is modelled using an explicit intermittency function in conjunction with the SA turbulence model – both are discussed in Section III.C.

Unlike the local  $\gamma-Re_\theta$  transport equation approach,<sup>22</sup> the other approaches are non-local in their formulation, which has some disadvantages. However, these issues are being addressed; for example, approaches 1 and 2 have been successfully parallelized and extended to three-dimensional flows by Krimmelbein *et al.*,<sup>10,29</sup> and there is no restriction to their use in an implicit Newton-Krylov type solver, as demonstrated in this work. There is also no required calibration specific to a particular turbulence model.<sup>24</sup> Furthermore, correlations for crossflow instabilities (such as the  $C_1$  criterion) have already been successfully combined with these approaches, with experimental validation demonstrating accurate transition prediction on transonic swept wings in three dimensions.<sup>15,16</sup> Finally, the modular implementation of the proposed transition prediction framework facilitates the use of higher fidelity methods (such as linear stability theory or the parabolized stability equations) if so desired.

## II.B. RANS-based Aerodynamic Shape Optimization for NLF

Research in the area of high-fidelity aerodynamic shape optimization with laminar-turbulent transition is sparse. The majority of research in this field employs inviscid-viscous coupling strategies, making use of boundary-layer codes for the viscous formulation and either a panel method or the Euler equations for the inviscid formulation.<sup>30,31,32,33,34,35,36,37</sup> Although the inviscid/viscous coupling strategies can be computationally cheaper than the higher-fidelity RANS solvers, the industry’s trend toward the use of RANS solvers strongly suggests that NLF design tools should follow suit. Recent research making use of RANS solvers to optimize with transition prediction has shown promising results.

Driver and Zingg<sup>21</sup> coupled a RANS optimization framework to the MSES inviscid/viscous solver for transition prediction. This was a stop-gap approach used to successfully demonstrate the potential for NLF design using RANS-based optimization. Lee and Jameson<sup>38</sup> have successfully coupled a RANS solver to a boundary-layer code and an  $e^N$  database method (making use of the Baldwin-Lomax turbulence model) for NLF design in two and three dimensions. The gradient calculations in their work did not include the transition prediction, and their optimizations focused on the elimination of shock-waves for reduced wave drag. Khayat-zadeh and Nadarajah<sup>39,40</sup> successfully extended the Langtry-Menter transport equation approach to an adjoint-based optimization framework in two dimensions, and applied the framework to the design of low Reynolds number NLF airfoils with separation bubbles. Design objectives investigated included the minimization of turbulent kinetic energy and the maximization of the lift-to-drag ratio. More recently, several researchers have employed the Langtry-Menter approach in conjunction with finite-difference gradient approximations or gradient-free methods for the design of NLF airfoils and wind turbine blades.<sup>41,42,43,44,45</sup> Previous work by Rashad and Zingg also made use of a finite-difference gradient approximation.<sup>27</sup>

There are several specific areas that require continued research and development and have significant room for improvement. The first is the direct use of high-fidelity RANS solvers as opposed to inviscid/viscous coupling strategies. The second is to optimize at higher Reynolds and Mach numbers (representative of

subsonic and transonic transport aircraft). A third is to optimize for more realistic and practical designs through the use of multipoint design optimizations that incorporate the off-design performance during the optimization cycle.<sup>46</sup> In the same vein, design objectives and constraints should aim to reflect the industry's aerodynamic design objectives. Often, design objectives are formulated specifically or primarily to delay transition. Design objectives based on indirect functions – such as N factor curves – run the risk of creating a gap between the design tool's capabilities and the actual objectives of manufacturers. Finally, in order to account for three-dimensional features such as sweep angle, taper ratio, and twist,<sup>47</sup> there is a need for continued development of NLF design tools applicable to full aircraft configurations in three dimensions. Ultimately, such design tools should include the prediction of transition due to crossflow instabilities, and they should incorporate the transition criteria into the evaluation of the objective, constraints and gradients of the design problem.

### III. Flow Solver Methodology

The steady RANS equations are solved in two dimensions using a second-order Newton-Krylov finite-difference flow solver (named Optima2D) originally developed by Nemec and Zingg.<sup>48,49</sup> The linear system that arises at each Newton iteration is solved using the preconditioned Generalized Minimum Residual (GMRES) method. Global convergence of the Newton method is made possible by an approximate factorization start-up algorithm. Numerical dissipation is added by either the scalar dissipation scheme of Jameson *et al.*<sup>50</sup> or the matrix dissipation scheme of Swanson and Turkel.<sup>51</sup> The turbulent eddy viscosity is computed using the one-equation Spalart-Allmaras (SA) turbulence model.<sup>52</sup> As mentioned, the SA model is not itself capable of predicting transition; the remaining constituents of the proposed transition prediction framework include: the determination of the boundary-layer edge and properties, the calculation and evaluation of the transition criteria, and the implementation of a robust iterative procedure for transition prediction in the RANS solver.

Three boundary-layer edge-finding methods have been implemented, verified and compared in the RANS flow solver; details may be in Rashad and Zingg.<sup>27</sup> The accuracy of the integrated boundary-layer properties has also been assessed through a detailed grid convergence study and by comparison to numerical boundary-layer properties obtained from XFOIL.<sup>27</sup> It was found that with reasonable grid density, the boundary-layer properties can be computed directly from the Navier-Stokes solution with sufficient accuracy. The remainder of this section presents the transition criteria and discusses their implementation in the RANS solver.

#### III.A. AHD Transition Criterion

The natural transition locations (due to Tollmien-Schlichting instabilities) are predicted using the new compressible form of the Arnal-Habiballah-Delcourt (AHD) criterion.<sup>18,15,16,53</sup> The AHD criterion is designed for low to moderate freestream turbulence intensities ( $T_u \leq 0.1\%$ ), as typically encountered in external aerodynamic cruise conditions for transport aircraft.<sup>18</sup> The method has the advantage of being applicable to a wide range of pressure gradients, as well as compressible flows.<sup>18</sup> It does not predict transition due to crossflow instabilities; however, it can be combined with other criteria (such as the C1 criterion) for that purpose.<sup>53</sup>

Beginning at the stagnation point, we march toward the trailing edge of the airfoil, treating the upper and lower surfaces independently. Our first task is to find the streamwise location of the neutral stability point,  $s_{cr}$ . Upstream of the neutral stability point, it is assumed (from linear stability theory) that all small disturbances over all frequencies remain stable and damp out. The neutral stability point is found using the *critical* Reynolds number, calculated as a function of the incompressible shape factor,  $H_{inc} = \delta_{inc}^*/\theta_{inc}$ , as

$$Re_{\theta_{cr}} = \exp \left[ \frac{E}{H_{inc}} - F \right], \quad (1)$$

such that  $s_{cr}$  is the first point at which, locally,  $Re_{\theta}=Re_{\theta_{cr}}$ . The incompressible shape factor is used even for compressible flow, as recommended by Cliquet *et al.*<sup>18</sup> The functions E and F are computed as a function of the Mach number at the boundary layer-edge, and may be found in the Appendix. Note that  $Re_{\theta_{cr}}$  typically decreases in the streamwise direction and is greater than  $Re_{\theta}$  upstream of the critical point.

The next step is to find the streamwise location of the laminar-turbulent transition point,  $s_{tr}$ . The transition criterion is computed and checked only at points downstream of the neutral stability point. The

AHD criterion uses the Falkner-Skan self-similar solutions to represent the laminar boundary-layer profiles, which are characterized by the local Pohlhausen number.<sup>18</sup> Following the work of Granville, the necessary relationships are extended from self-similar boundary-layers to actual flows by replacing  $\Lambda_2$  with its mean value as follows:<sup>18</sup>

$$\Lambda_2 = \frac{\theta^2}{\nu} \frac{dU_e}{ds} \implies \overline{\Lambda_2} = \frac{1}{s - s_{cr}} \int_{s_{cr}}^s \Lambda_2 ds. \quad (2)$$

Arnal *et al.* proposed the following expression for the transitional Reynolds number,  $Re_{\theta_{tr}}$ :

$$Re_{\theta_{tr}} = Re_{\theta_{cr}} + A \cdot \exp(B \cdot \overline{\Lambda_2}) \left[ \ln(C \cdot T_u) - D \cdot \overline{\Lambda_2} \right], \quad (3)$$

where  $T_u$  is the freestream turbulence level, and the functions A, B, C, and D may be found in the Appendix. The transition point is then taken as the first point at which, locally,  $Re_{\theta} = Re_{\theta_{tr}}$ . Note that  $Re_{\theta_{tr}}$  typically decreases in the streamwise direction and is greater than  $Re_{\theta}$  upstream of the transition point.

### III.B. Simplified $e^N$ envelope method

The simplified  $e^N$  envelope method used in Drela's XFOIL and MSES codes<sup>28</sup> has also been incorporated. The method makes direct use of the boundary-layer properties to approximate the envelope of the spatial amplification rates of the disturbances (the N-factors), as opposed to actually solving the linear stability equations. While the envelope method does not track individual frequencies, it is significantly more efficient.<sup>17</sup> The correlations are based on linear stability results for the Falkner-Skan family of velocity profiles. The envelopes of the growth rates are locally approximated as straight lines with respect to the streamwise direction,  $\xi$ , as follows:<sup>28</sup>

$$\frac{dN}{d\xi} = \text{fcn}(H_k, \theta) = \frac{dN}{dRe_{\theta}} \cdot \frac{m+1}{2} \cdot l \cdot \frac{1}{\theta}, \quad (4)$$

where  $\frac{dN}{dRe_{\theta}}$ ,  $m$ , and  $l$  are functions of the so-called kinematic shape factor,  $H_k$ , and may be found in the Appendix. The kinematic shape factor is computed based on the incompressible shape factor,  $H_{inc}$ , and the Mach number at the boundary-layer edge,  $M_e$ , as

$$H_k = \frac{H_{inc} - 0.290M_e^2}{1 + 0.113M_e^2}. \quad (5)$$

The N-factor envelope is then obtained by integrating Equation (4) in the streamwise direction, beginning at the critical point. The critical point is the first point at which, locally,  $Re_{\theta} = Re_{\theta_{cr}}$ , where  $Re_{\theta_{cr}}$  is defined by<sup>28</sup>

$$\log_{10} Re_{\theta_{cr}} = \left( \frac{1.415}{H_k - 1} - 0.489 \right) \tanh \left( \frac{20}{H_k - 1} - 12.9 \right) + \frac{3.295}{H_k - 1} + 0.44. \quad (6)$$

### III.C. RANS Implementation

#### III.C.1. Iterative Transition Prediction Procedure

Automatic transition prediction in the RANS solver is achieved through an iterative process, similar to that developed by several researchers.<sup>6, 11, 18, 17, 20, 53</sup> This section provides an overview of the present implementation.

An initial guess of the transition locations (top and bottom surfaces) is required and is typically taken at 25% chord. Transition is then forced to occur at the initial locations using a transition region model (Section III.C.2). When the magnitude of the flow residual has been reduced to  $5 \times 10^{-6}$ , the transition prediction module is invoked to process the RANS solution; the tight tolerance was chosen to ensure sufficiently accurate boundary-layer properties for transition prediction. The forced transition points are then moved upstream or downstream as required toward the predicted transition points in an under-relaxed fashion,<sup>20</sup> such that

$$X_f^{\text{new}} = X_f^{\text{old}} - \omega (X_f^{\text{old}} - X_p), \quad (7)$$

where  $\omega$  is the under-relaxation factor, and  $X_f$  and  $X_p$  represent the normalized chord locations of the forced and predicted transition points, respectively. When the flow residual returns to a magnitude of  $5 \times 10^{-6}$ , the



predicted and forced transition points are again updated. The iterative transition prediction procedure is considered converged when the absolute value of the *transition residual*,  $|R_{tr}|=|X_f - X_p|$ , has converged to a tolerance of  $\epsilon_{tp}$ . When the transition prediction procedure has converged,  $X_f$  is set equal to  $X_p$ , and the flow solver continues to converge until the magnitude of the flow residual has reduced to a tolerance of  $\epsilon_r$ . For the purposes of gradient-based aerodynamic shape optimization,  $\epsilon_{tp}$  and  $\epsilon_r$  are set to  $10^{-8}$  and  $10^{-12}$ , respectively, ensuring a sufficiently smooth design space for optimization.

From numerical experimentation, an under-relaxation factor of  $\omega = 0.8$  has been selected as a good compromise between efficiency and robustness. A linear extrapolation of the boundary-layer properties – from the laminar region into the turbulent region – allows the transition criterion to predict transition downstream of the forced transition points (when required). If laminar flow separation is detected and a transitional separation bubble forms, the  $e^N$  envelope method is able to predict the transition location in the separation bubble.<sup>28</sup> When using the AHD criterion, the laminar separation point is simply taken as the transition point. A robust logic has been determined through extensive numerical experimentation and code verification to handle the various outcomes of the transition prediction module. For the various airfoils and flight conditions investigated, it was found that the iterative transition prediction procedure requires approximately three to four times the computational cost of a fully-turbulent flow solve, with no significant addition to the memory requirements.

### III.C.2. Modelling of Transitional Flow Regions

The transition to turbulence is enforced in the Navier-Stokes solution by one of two methods. The first makes use of the trip term and the  $f_{t1}$  and  $f_{t2}$  trip functions in the SA model, as published by Spalart and Allmaras.<sup>52</sup> The second approach makes use of an intermittency function that scales the turbulent eddy viscosity, such that  $\mu_t = \gamma \mu_{t0}$  and  $0 \leq \gamma \leq 1$ , as used by Cliquet *et al.*<sup>18</sup> The intermittency function has been defined to take the form of an S-type curve with a smooth initial ramp-up, such that

$$\gamma(x) = \exp(-5 \xi^2), \quad \text{where} \quad \xi = 1 + \frac{x_{tr}^{beg} - x}{l_{tr}}, \quad (8)$$

$x_{tr}^{beg}$  represents the beginning of the transitional flow region as predicted by the transition criterion, and  $l_{tr}$  is the transition length. Although there are no physics-based methods for determining the transition length,<sup>17</sup> empirically correlated approximations have been developed that make use of the boundary-layer properties at the transition point. Following the work of Krumbein,<sup>54</sup> the transition length can be obtained from

$$Re_{l_{tr}} = 4.6 (Re_{\delta_{tr}^*})^{1.5}. \quad (9)$$

For a smooth ramp-up of the eddy viscosity, the transition region must be sufficiently resolved; failure to do so was observed to cause noise in the design space during optimization. A comparison of the eddy viscosity ramp-up using the intermittency function as compared to the Spalart-Allmaras trip terms may be found in Rashad and Zingg.<sup>27</sup>

## IV. Optimization Framework

The goal of the aerodynamic shape optimization framework is to minimize the specified design objective,  $J$ , with respect to the design variables,  $X$ , subject to linear and nonlinear constraints. Although the optimizer can handle several different design objectives, such as the maximization of lift-to-drag ratio or endurance factor, in this work the focus is on lift-constrained drag minimization. The proposed optimization framework consists of the following: (i) a two-dimensional RANS flow solver (described in the preceding section), (ii) a geometry parametrization and mesh movement algorithm, (iii) a sequential quadratic programming algorithm, and (iv) a discrete-adjoint gradient computation.

The airfoil geometry is parametrized using B-splines, the details of which may be found in Nemec and Zingg.<sup>48</sup> The design variables,  $X$ , are defined as the  $y$ -coordinates of the B-spline control points; the control points are free to move in the vertical direction to facilitate shape changes during the optimization cycle. The angle of attack of the airfoil is an additional design variable. The algebraic grid-perturbation strategy described in Nemec and Zingg<sup>48</sup> is used to ensure that the computational grid is smoothly adjusted to conform to the changing geometric configurations.

The SNOPT general purpose Sequential Quadratic Programming (SQP) algorithm – developed by Gill *et al.*<sup>55</sup> – is employed as the optimizer in this work. SQP methods are among the most effective gradient-based approaches for treating smooth, nonlinearly constrained optimization problems.<sup>56</sup> SNOPT solves problems that are locally optimal by minimizing quadratic models of the augmented Lagrangian.<sup>55</sup> A backtracking line-search strategy is used to determine the step-size and update the design variables in a manner that ensures a sufficient decrease in the augmented Lagrangian merit function. The Hessian of the Lagrangian is approximated using the quasi-Newton method of Broyden, Fletcher, Goldfarb, and Shanno (BFGS). SNOPT requires the gradients of the objective function and constraints; ensuring sufficiently accurate gradients is of paramount importance to the success of the SQP algorithm. Two methods for computing accurate gradients (that incorporate the sensitivities of the transition criterion) have been implemented; a parallel finite-difference gradient evaluation,<sup>27</sup> along with a new augmented discrete-adjoint gradient evaluation, presented in the next section.

#### IV.A. Discrete-Adjoint Gradient Evaluation

The principal advantage of the adjoint method is that its cost does not scale with the number of design variables, but rather with the number of objectives and nonlinear constraints. Hence, the objective function gradient evaluation only requires one flow solve and one adjoint solve; for lift-constrained drag minimizations, an additional adjoint solve is required for the gradient of the lift-constraint. A detailed description and derivation of the discrete-adjoint formulation in the context of aerodynamic shape optimization may be found in Nemec and Zingg.<sup>48</sup>

In the discrete-adjoint approach, the gradient is evaluated using the following expression:<sup>48</sup>

$$G = \frac{dJ}{dX} = \frac{\partial J}{\partial X} - \psi^T \frac{\partial R}{\partial X}, \quad (10)$$

where  $R = R[X, Q(X)]$  represents the discretized RANS residual vector. The vector of adjoint variables,  $\psi$ , is obtained by solving the linear system of equations given by

$$\frac{\partial R^T}{\partial Q} \psi = \frac{\partial J^T}{\partial Q}, \quad (11)$$

where  $Q$  is the vector of conserved flow variables.

##### IV.A.1. Adjoint Formulation for Transition Prediction

The AHD and  $e^N$  transition criteria (described in Sections III.A and III.B, respectively) are non-local in their formulation. As such, special consideration must be taken when evaluating and deriving an adjoint formulation capable of incorporating their sensitivities. The proposed approach is to append a new adjoint vector,  $\psi_{tr}$ , to the original adjoint vector, such that  $\bar{\psi} \Rightarrow [\psi; \psi_{tr}]$ . Henceforth, the overbar shall be used to indicate an augmented vector. The length of  $\psi_{tr}$  corresponds to the number of transition points,  $N_{tr}$ , which is equal to two for a single-element airfoil. For 3D wing configurations, the transition lines may be defined by a spanwise distribution of transition points;<sup>11</sup> the total number of spanwise transition points on all surfaces gives  $N_{tr}$ .

To compute the new adjoint variables, we specify a corresponding number of new residual equations, such that  $\bar{R} \Rightarrow [R; R_{tr}]$ . The new transition residual equations represent the distance between the forced and predicted transition locations,  $R_{tr} = X_f - X_p$ , as described in Section III.C.1. The transition residual vector is satisfied ( $R_{tr} = 0$ ) when the forced transition points are in locations consistent with the given transition criterion ( $X_f = X_p$ ).

In addition, the vector of conserved flow variables must be augmented to include the forced transition locations, such that  $\bar{Q} \Rightarrow [Q; X_f]$ . Finally, the entire adjoint vector,  $\bar{\psi}$ , is computed by solving the augmented

linear system of equations given by

$$\frac{\partial \bar{R}}{\partial Q}^T \bar{\psi} = \frac{\partial J}{\partial Q}^T \mapsto \begin{bmatrix} \frac{\partial R}{\partial Q} & \frac{\partial R}{\partial X_f} \\ \text{---} & \text{---} \\ \frac{\partial R_{tr}}{\partial Q} & \frac{\partial R_{tr}}{\partial X_f} \end{bmatrix}^T \begin{bmatrix} \psi \\ \psi_{tr} \end{bmatrix} = \begin{bmatrix} \frac{\partial J}{\partial Q} \\ \text{---} \\ \frac{\partial J}{\partial X_f} \end{bmatrix}^T. \quad (12)$$

The  $\frac{\partial R}{\partial X_f}$  matrix represents the sensitivity of the flow residual to the forced transition points. It is computed efficiently using a centered difference approximation requiring only two evaluations of the flow residual for each transition point. The matrix  $\frac{\partial R_{tr}}{\partial X_f}$  represents the sensitivity of the transition residual to the forced transition points, which by the definition of  $R_{tr}=X_f-X_p$ , is simply the  $N_{tr} \times N_{tr}$  identity matrix. Furthermore, the vector  $\frac{\partial J}{\partial X_f}$  is simply the null vector for typical objectives and constraints such as lift and drag, since these objectives do not depend explicitly (but rather implicitly) on the transition points. The matrix  $\frac{\partial R_{tr}}{\partial Q}$  is by far the most complex of the new matrices in the augmented formulation as it represents the sensitivity of the transition residual (including the evaluation of the boundary-layer edge, the boundary-layer properties, and the given transition criterion) to the conserved flow variables. This matrix is computed accurately using a complex-step approximation<sup>57,58</sup> discussed further below.

The proposed approach has several advantages. First and foremost, the sensitivities of the given transition criterion with respect to the design variables are explicitly incorporated into the adjoint gradient, in turn allowing the optimizer to exploit that information. Second, the non-locality in the given transition criterion is confined to the last  $N_{tr}$  rows of the new Jacobian matrix,  $\frac{\partial \bar{R}}{\partial Q}$ . Note that the new adjoint system is only slightly larger than the original system, since the number of additional rows in the new Jacobian is only  $N_{tr}$ . Thus, the use of the complex-step approximation in the calculation of  $\frac{\partial R_{tr}}{\partial Q}$  does not incur significant additional expense. Furthermore, the specific nodes involved in satisfying the transition criteria (i.e. from the critical point to the transition point, and from the airfoil surface to the boundary-layer edge) are known; thus, only that subset of nodes is perturbed when using the complex-step approximation to evaluate  $\frac{\partial R_{tr}}{\partial Q}$ . Third, no extra work is needed to incorporate the sensitivities of a new or different user-specified transition criterion. Fourth, the iterative procedure used to determine the final forced transition locations, as described in Section III.C, need not be explicitly included, since the converged RANS solution satisfies the transition criterion,  $R_{tr}=0$ , and the sensitivities of the given transition criterion are included by the addition of the new adjoint variables. Fifth, the sensitivities of  $R$  and  $J$  with respect to  $X_f$  (that is,  $\frac{\partial J}{\partial X_f}$  and  $\frac{\partial R}{\partial X_f}$ ) need not contain any information about the transition criterion. Finally, the linear system of equations given by (12) may be solved using the same preconditioned GMRES approach used for the original adjoint formulation.

#### IV.A.2. Solving the Augmented Adjoint System

An iterative approach that makes use of the Generalized Minimum Residual (GMRES) Krylov subspace solver is proposed to solve the augmented adjoint system. The solution procedure requires an initial guess for the transition adjoint variables, taken as  $\psi_{tr}^{n=1} = 0$ , and is summarized as follows:

1. Use preconditioned GMRES to solve the following linear system of equations for  $\psi^{n+1}$ , where  $n$  is the iteration counter:

$$\frac{\partial R}{\partial Q}^T \psi^{n+1} = \frac{\partial J}{\partial Q}^T - \frac{\partial R_{tr}}{\partial Q}^T \psi_{tr}^n. \quad (13)$$

2. Update the  $\psi_{tr}$  vector by solving the following linear system of equations (directly):

$$\frac{\partial R_{tr}}{\partial X_f}^T \psi_{tr}^{n+1} = \frac{\partial J}{\partial X_f}^T - \frac{\partial R}{\partial X_f}^T \psi^{n+1}. \quad (14)$$

Note that since  $\frac{\partial R_{tr}}{\partial X_f}$  is the identity matrix and  $\frac{\partial J}{\partial X_f}$  is the null vector, (14) simplifies to

$$\psi_{tr}^{n+1} = -\frac{\partial R}{\partial X_f}^T \psi^{n+1}. \quad (15)$$



3. Increment the iteration counter,  $n \leftarrow n + 1$ , and return to step 1.
4. Stop when a given convergence criterion is satisfied. The convergence criterion selected for the iterative procedure makes use of the L2-norm of the augmented adjoint system, such that

$$\left\| \frac{\partial \bar{R}}{\partial \bar{Q}}^T \bar{\psi} - \frac{\partial J}{\partial \bar{Q}} \right\|_2 \leq \epsilon_{\text{adj}}. \quad (16)$$

A value of  $\epsilon_{\text{adj}} = 10^{-8}$  has been selected to ensure that the final solution vector,  $\bar{\psi}$ , satisfies the augmented system of equations sufficiently well.

One of the main advantages of the proposed iterative approach is that, in step 1, the same first-order preconditioner used to precondition GMRES during the flow solution (and the original adjoint solution) can also be used here to precondition the system given by (13). Furthermore, in the above algorithm GMRES makes use of the same left-hand side during each iteration, with only the right-hand side being modified. It follows that the robustness of GMRES that has been observed in fully-turbulent and fixed transition flow solutions is preserved here. Another advantage is that the method is easy to implement since it uses the same matrix-vector products in step 1 as the fully-turbulent and fixed transition solutions, and it requires no modifications within the GMRES solver itself. A principal disadvantage of the iterative approach is the time required to solve (13) multiple times. However, with the appropriate selection of an initial guess and by the under-relaxation of the updates, the method is relatively quick to converge, typically requiring between 5 and 10 iterations. For example, it has been observed that the time required to compute the gradients for a lift-constrained drag minimization (both  $\partial C_d / \partial X$  and  $\partial C_l / \partial X$ ) using the proposed algorithm is equal to or less than the time required to compute a single flow solution with free transition.

#### IV.B. Multipoint Optimization

We use multipoint optimization to ensure that our aerodynamic designs perform reasonably well over a given flight envelope. This is particularly important in the design of NLF airfoils, which, in order to maximize the extent of laminar flow, tend to take the boundary-layer very close to the point of separation prior to pressure recovery. As such, the off-design performance of NLF airfoils must be considered during the design process to ensure practical and robust designs. We use the methodology of Buckley and Zingg<sup>59,46</sup> to perform multipoint optimization capable of handling a comprehensive set of aerodynamic design requirements. In particular, we are interested in considering a range of Reynolds numbers, Mach numbers, and aircraft weights ( $W$ ). We keep the cruise altitude constant in this work (however it can also be included) and by specifying a range of Mach numbers and aircraft weights, we can obtain the corresponding range of Reynolds numbers and lift requirements. The optimizer then minimizes the weighted integral of the objective (in our case, the drag coefficient) subject to the lift constraints (one for each design point). Also note that each operating point has an associated angle of attack, all of which are included as additional design variables. The weighted integral is defined as<sup>46</sup>

$$\int_{W_1}^{W_2} \int_{M_1}^{M_2} C_d(M, W) \mathcal{Z}(M, W) dM dW \quad (17)$$

where  $\mathcal{Z}$  is a weighting function to be specified by the designer. This weighting function allows the designer to specify the importance of each design point according to their own priorities. The objective function,  $J$ , is an approximation to (17) given by

$$\mathcal{J} = \sum_{i=1}^{N_W} \sum_{j=1}^{N_M} \mathcal{T}_{i,j} C_d(M_i, W_j) \mathcal{Z}(M_i, W_j) \Delta M \Delta W, \quad (18)$$

where  $N_M$  and  $N_W$  are the numbers of quadrature points, and  $\Delta M$  and  $\Delta W$  are the corresponding spacings between quadrature points. The  $\mathcal{T}_{i,j}$  are the associated quadrature weights used to approximate the integral. In this work, the trapezoidal quadrature rule is employed.

The above multipoint formulation requires one flow solution and two adjoint solutions for each operating point. Buckley and Zingg<sup>46</sup> have parallelized the multipoint framework such that multiple processors compute the necessary objective, constraint, and gradient information. This approach has been shown to be an effective technique for robust and efficient aerodynamic design over a range of operating conditions.<sup>59,46</sup> Full details of the various operating conditions and their associated weights are presented in Section V.G.

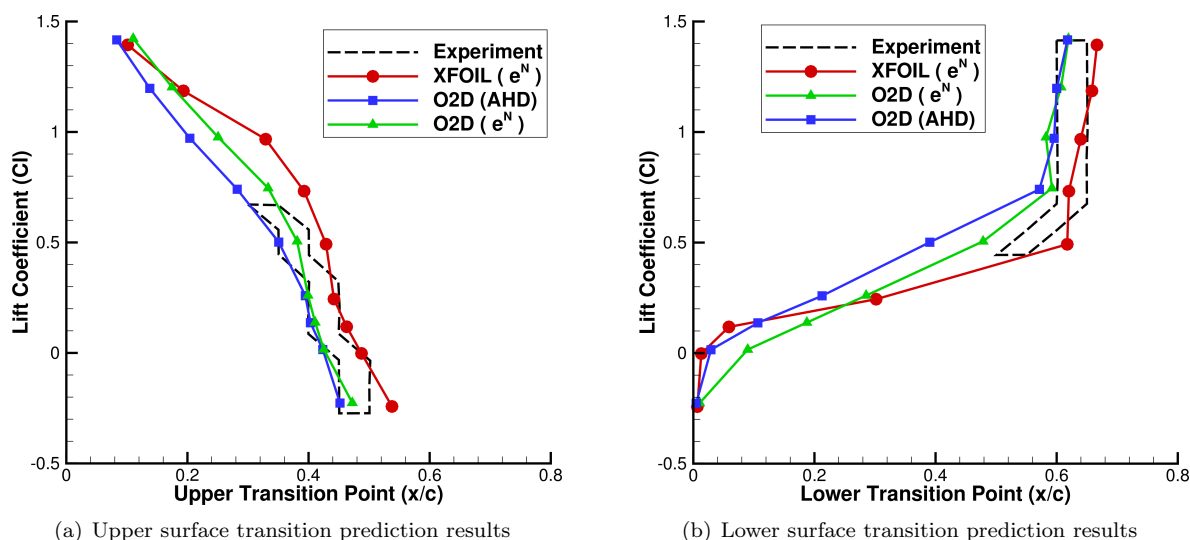


Figure 1. NLF-0416 transition prediction validation

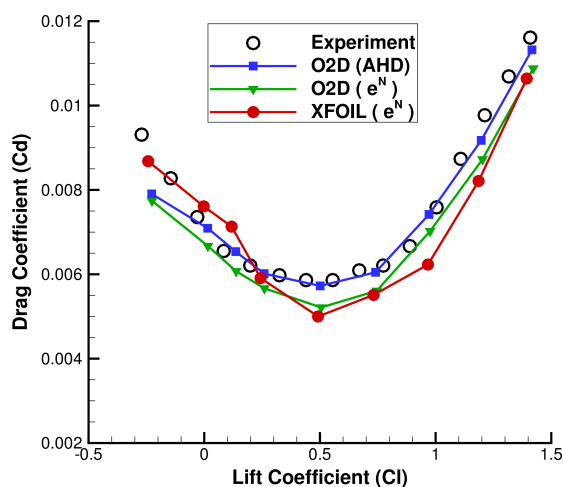


Figure 2. NLF-0416 drag polar comparison

## V. Results

### V.A. Transition Prediction

The transition prediction capabilities of the flow solver are validated by comparison to experimental transition data for the NLF-0416 airfoil developed by Somers.<sup>60</sup> The experimental results for NLF-0416 were obtained in the Langley Low Turbulence Pressure Tunnel (LTPT) using microphoned pressure taps.<sup>60</sup> The resolution of the experiments corresponds to the physical spacing of the microphoned taps along the chord of the airfoil.

The test case results are for a  $449 \times 385$  C-grid around the NLF-0416 airfoil at  $Re = 4 \times 10^6$ ,  $M = 0.2$ , and  $T_u = 0.1\%$  (and  $N = 8$  for XFOIL). The transition points predicted by both Optima2D and XFOIL are presented in Figure 1, along with the wind tunnel experimental data. The results of this test case show that the predictive capabilities of Optima2D match closely with the published experimental results over a range of lift coefficients. Figure 2 presents the drag polar for the NLF-0416 airfoil using both Optima2D and XFOIL. Good agreement is observed between the experimental results and the predicted transition locations and drag polar computed using Optima2D. In Somers' report,<sup>60</sup> the freestream turbulence intensity,  $T_u$ , was unfortunately not published for the NLF-0416 experiments. It is possible that the wind tunnel may have had lower or higher  $T_u$  than the  $0.1\%$  used for the computations. Further verification and validation results may be found in Rashad and Zingg.<sup>27</sup>

Table 1. Optimization cases

Case	Aircraft	Reynolds Number ( $Re$ )	Mach Number ( $M$ )	Lift Coefficient ( $C_l^*$ )
A	Cessna 172R	$5.6 \times 10^6$	0.19	0.30
B	Dash-8 Q400	$15.7 \times 10^6$	0.60	0.42
C	Boeing 737-8	$20.3 \times 10^6$	0.71	0.50

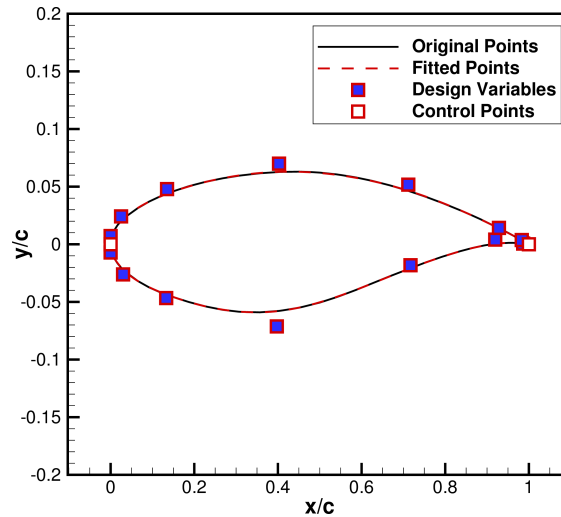


Figure 3. RAE-2822 B-spline parameterization

## V.B. Optimization Results - Problem Definitions

To demonstrate the NLF design capabilities of the optimization framework, single and multipoint optimizations are performed at conditions associated with subsonic and transonic commercial aircraft. The objective is to minimize the total drag of the airfoil constrained by a user-specified lift target,  $C_l^*$ . For structural considerations, additional inequality constraints are included. An area constraint ensures that the final area of the airfoil is greater than or equal to the initial area, and a thickness constraint near the leading edge ensures a minimum thickness of 2.5% chord located at 2.7% chord.

Single-point optimization results are presented for all of the cases outlined in Table 1. Cases A, B, and C were selected to approximate the cruise flight conditions of the Cessna 172R, the Bombardier Dash-8 Q400, and the Boeing 737-800, respectively. Multipoint optimization is performed on the Dash-8 Q400 and is presented in section V.G.

The initial geometry for all cases is the RAE-2822 airfoil parametrized by seventeen B-spline control points, as shown in Figure 3. The control point located at the leading edge of the airfoil, as well as the two coincident control points at the trailing edge, are kept fixed throughout the optimization. The  $y$ -coordinates of the remaining 14 control points are used as the geometric design variables (shaded in blue). The angle of attack is also included as an additional design variable. The computational grid consists of a  $575 \times 224$  C-grid, resulting from grid convergence studies on the boundary-layer properties, with flow solutions computed using the scalar dissipation scheme of Jameson *et al.*<sup>50</sup> All results were obtained using the compressible Bernoulli edge-finding method, the intermittency function transition region model, the discrete-adjoint based gradient evaluation, and the  $e^N$  transition criterion. The full paper will present a comparison to optimizations performed with the AHD transition criterion. Prior to discussing the optimization results, the next section presents an accuracy assessment of the discrete-adjoint gradient evaluation.

## V.C. Verification of Discrete-Adjoint Gradient

In order to verify the accuracy of the augmented adjoint formulation, we compare the resulting gradient vector to a finite-difference gradient vector. If the correct step size is selected, then each component of the

**Table 2.** Comparison of finite-difference (FD) and discrete-adjoint (AD) gradient components

Component	FD	AD	Diff. (AD–FD)	% Diff.
1	0.0679450100	0.0679451512	1.4123964E-07	0.0002078735
2	0.0219869160	0.0219869646	4.8564238E-08	0.0002208779
3	0.0097466881	0.0097466700	-1.8115582E-08	-0.0001858640
4	0.0175834070	0.0175834517	4.4744770E-08	0.0002544716
5	-0.0193916140	-0.0193916634	-4.9418155E-08	0.0002548429
6	-0.0299716320	-0.0299718445	-2.1254895E-07	0.0007091671
7	-0.0047241138	-0.0047240276	8.6154773E-08	-0.0018237235
8	0.2247156100	0.2247165247	9.1469697E-07	0.0004070465
9	-0.0356937590	-0.0356938516	-9.2638314E-08	0.0002595364
10	-0.0754516680	-0.0754518118	-1.4383642E-07	0.0001906339
11	0.0093773201	0.0093772871	-3.2993728E-08	-0.0003518460
12	0.0212247700	0.0212248201	5.0099786E-08	0.0002360440
13	0.0298430110	0.0298430441	3.3118203E-08	0.0001109747
14	0.0423508340	0.0423509102	7.6172428E-08	0.0001798605
AoA	0.0010081208	0.0010081334	1.2597056E-08	0.0012495582

gradient vectors should be equal to within a small tolerance. For this accuracy assessment we perform a single iteration of the optimization to obtain the discrete-adjoint gradient (that is, the sensitivity of the drag coefficient to the design variables) for the initial geometry and parameterization described in Section V.B, under the flight conditions of Case B. We also perform a centered-difference approximation by perturbing each design variable individually using a step-size of  $1 \times 10^{-6}$ . Table 2 compares the resulting adjoint (AD) and finite-difference (FD) gradient vectors for all design variables; the first 14 components are the geometric design variables, the last is the angle of attack. The results demonstrate excellent agreement between the two methods for computing the gradient, with the finite-difference gradient requiring 30 flow solutions, compared to a single flow solution (and a single adjoint solution) required for the adjoint gradient. The gradients of the nonlinear lift constraint show slightly better agreement and are omitted for brevity. Further gradient accuracy verifications have been carried out at different flight conditions and geometries, with similar results. Having verified the feasibility of the augmented adjoint formulation for transition prediction and the accuracy of its resulting gradient, the remainder of this paper is devoted to the presentation of the single and multipoint optimization results obtained using the discrete-adjoint gradient.

#### V.D. Case A Results: $Re = 5.6 \times 10^6$ , $M = 0.19$ , $C_l^* = 0.3$

The Cessna 172R is assumed to be cruising at 6000 ft, a speed of 120 knots and a weight of 2200 lbs. The results were obtained using the  $e^N$  envelope transition criterion with  $N_{\text{crit}}=9$ . In Table 3, a summary of the results comparing the initial and optimized airfoils is presented. Figure 4(a) compares the initial and optimized geometries, and Figure 4(b) compares the pressure profiles. The transition locations are indicated by the solid circles. The angle of attack increased from an initial value of  $0.69^\circ$  to  $0.83^\circ$ , the lift constraint is satisfied, and the total drag is reduced by 22.3 drag counts, or 46%. The ability of the optimizer to exploit the laminar-turbulent transition prediction is made evident by the aft movement of the transition points from 49% to 81% chord on the upper surface and 54% to 85% chord on the lower surface. The leading edge radius has decreased, and the point of maximum thickness has been pushed significantly aft in order to extend the region of favourable pressure gradient.

#### V.E. Case B Results: $Re = 15.7 \times 10^6$ , $M = 0.60$ , $C_l^* = 0.42$

The design point for the Dash-8 Q400 is taken as point 6 from the multipoint optimization case (discussed in Section V.G). The results are obtained using the  $e^N$  envelope transition criterion with  $N_{\text{crit}}=9$ . Table 4 provides a summary of the results comparing the initial and optimized airfoils. In this case, the angle of

**Table 3. Case A summary of optimization results:**  $Re = 5.6 \times 10^6$ ,  $M = 0.19$ ,  $C_l^* = 0.3$

	$C_d$	$C_{d_p}$	$C_{d_v}$	$C_l$	$C_m$	$T_{up}(x/c)$	$T_{lo}(x/c)$	$AoA$
Initial	0.00482	0.00083	0.00399	0.3000	-0.06797	0.4918	0.5371	0.6858°
Optimized	0.00259	0.00062	0.00196	0.3004	-0.05472	0.8085	0.8500	0.8312°

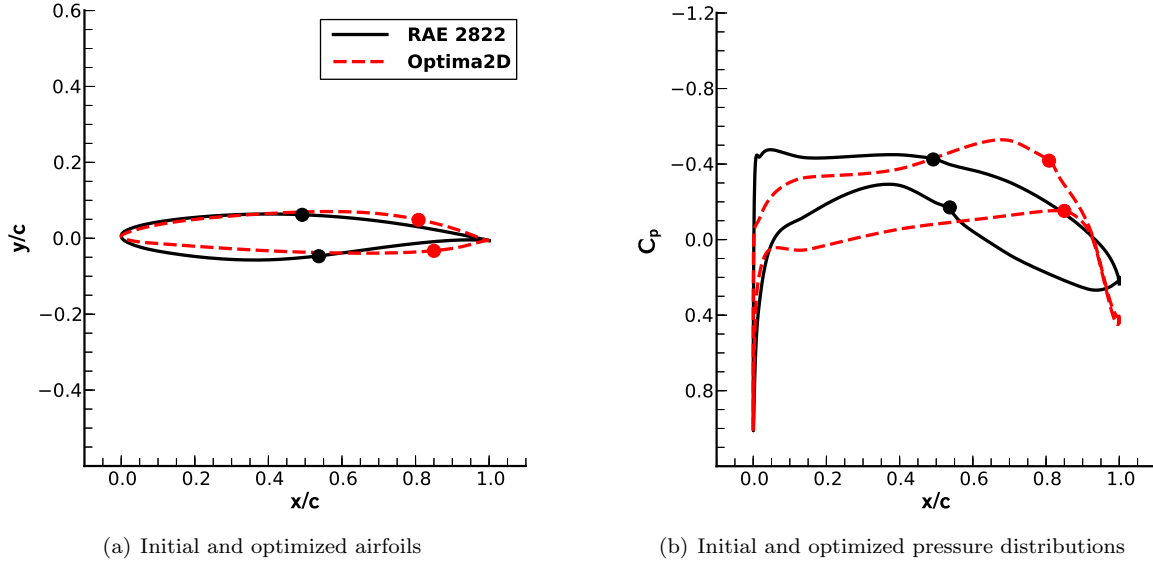


**Figure 4. Case A optimization results:**  $Re = 5.6 \times 10^6$ ,  $M = 0.19$ ,  $C_l^* = 0.3$ ; symbols indicate transition point locations

attack is decreased from an initial value of  $1.14^\circ$  to  $0.30^\circ$ , the lift constraint is again satisfied, and the total drag is reduced by 31.2 drag counts, or 53%. The transition point on the upper surface has been moved aft by over 50% chord, while the lower surface transition point has moved aft approximately 20% chord.

Figure 5(a) compares the initial and optimized geometries; Figure 5(b) compares the pressure profiles. It can be observed that the optimizer was again successful in designing an airfoil with an extended favourable pressure gradient on both the upper and lower surfaces. As in the previous case, the optimized geometry has a smaller leading edge radius, and the location of maximum thickness has been moved aft. These results demonstrate the ability of the optimizer to design new NLF airfoils which would typically require considerable aerodynamic experience to design.

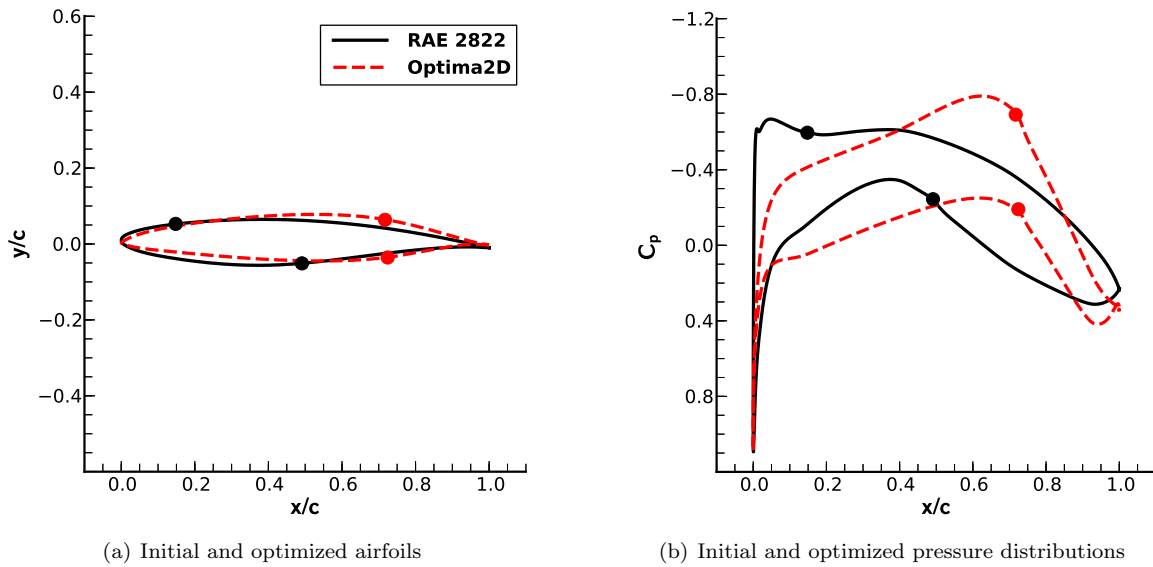
#### V.F. Case C Results: $Re = 20.3 \times 10^6$ , $M = 0.71$ , $C_l^* = 0.50$

The Boeing 737-800 has a wing sweep angle of  $25^\circ$  and is assumed to be cruising at 35000 ft and a Mach number of 0.785, which corresponds to an effective Mach number of 0.71. The target lift coefficient is 0.5. Results are obtained using the  $e^N$  envelope transition criterion with  $N_{crit}=9$ . Due to the transonic flight conditions, the optimization in this case is less robust. The flow solver may fail to converge if the transition locations are moved aft of a shockwave during the transition prediction procedure, in turn causing unsteady flow separation. Modification to the transition prediction algorithm includes a more gradual movement of the transition locations, restricted to a maximum of 5% chord at each update. It is also recommended to start with initial transition locations that are well upstream of any potential shock waves; an initial guess of 25% chord is used here for both the upper and lower surfaces.

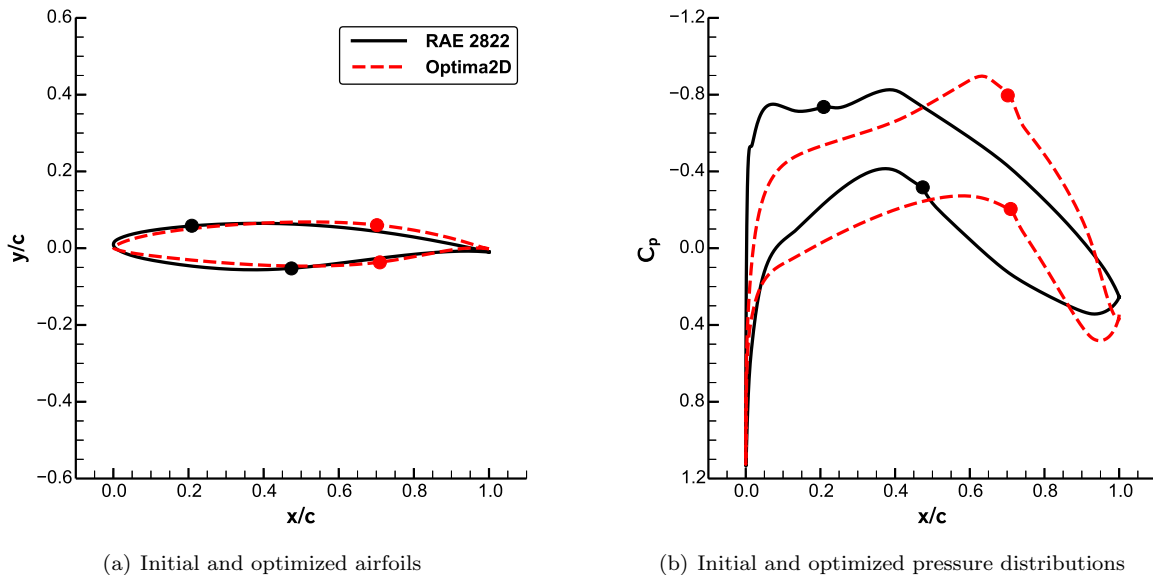
Table 5 provides a summary of the results comparing the initial and optimized airfoils. The angle of attack in this case is decreased from an initial value of  $1.13^\circ$  to  $0.15^\circ$ , the lift constraint is satisfied, and the total drag is reduced by 29 drag counts, or 47%. The transition points are moved from 20% to 70% chord on the upper surface, and from 47% to 71% chord on the lower surface. Figure 6(a) compares the initial and optimized geometries; Figure 6(b) compares the pressure profiles. In this case, the optimizer is successful in designing a shock-free, natural-laminar-flow airfoil, in turn, significantly reducing the total drag.

**Table 4. Case B summary of optimization results:**  $Re = 15.7 \times 10^6$ ,  $M = 0.60$ ,  $C_l^* = 0.42$ 

	$C_d$	$C_{d_p}$	$C_{d_v}$	$C_l$	$C_m$	$T_{up}(x/c)$	$T_{lo}(x/c)$	$AoA$
Initial	0.00598	0.00194	0.00405	0.4200	-0.08129	0.1480	0.4912	$1.1424^\circ$
Optimized	0.00279	0.00089	0.00189	0.4197	-0.09629	0.7171	0.7243	$0.3013^\circ$

**Figure 5. Case B optimization results;**  $Re = 15.7 \times 10^6$ ,  $M = 0.60$ ,  $C_l^* = 0.42$ ; symbols indicate transition point locations**Table 5. Case C summary of optimization results:**  $Re = 20.3 \times 10^6$ ,  $M = 0.71$ ,  $C_l^* = 0.50$ 

	$C_d$	$C_{d_p}$	$C_{d_v}$	$C_l$	$C_m$	$T_{up}(x/c)$	$T_{lo}(x/c)$	$AoA$
Initial	0.00617	0.00259	0.00358	0.5000	-0.09427	0.2088	0.4740	$1.1292^\circ$
Optimized	0.00327	0.00144	0.00182	0.5001	-0.12827	0.7018	0.7095	$0.1545^\circ$

**Figure 6. Case C optimization results;**  $Re = 20.3 \times 10^6$ ,  $M = 0.71$ ,  $C_l^* = 0.50$ ; symbols indicate transition point locations



## V.G. Case B: Multipoint Optimization

Here we consider a multipoint optimization at a range of cruise conditions associated with the Dash-8 Q400 aircraft. A nine-point stencil, presented in Table 6, is defined by varying the aircraft weight and Mach number. This is done to reduce the sensitivity of the final optimized shape to variations in the flight conditions encountered during cruise and to enable efficient operation within this envelope. The aircraft is assumed to have a take-off weight equal to the Q400's maximum take-off weight of 64500 lbs. Given a typical payload, the usable fuel on board (at take-off) is approximated to be 7500 lbs. The three aircraft weights considered in the multipoint stencil are calculated from a 10%, 50% and 90% fuel burn, which loosely approximates the beginning, middle, and end of cruise. The three Mach numbers considered are 0.6, 0.54, and 0.48, which roughly correspond to high-speed, intermediate, and long-range design speeds of the Q400, respectively. Given the range of weights and Mach numbers, and assuming a constant cruising altitude of 23000 ft, we can then compute the corresponding range of Reynolds numbers and lift constraints presented in Table 6.

Recall from Section IV.B that the design objective given by (18) is an approximation to the weighted integral given by (17). Although any design priority weighting may be selected as desired, here we make the assumption that all design points are of equal importance, that is,  $\mathcal{Z}(W_i, M_j)=1$  for all  $i$  and  $j$ . Table 6 also presents the quadrature weights  $\mathcal{T}$  used to approximate (17) using the trapezoidal quadrature rule.

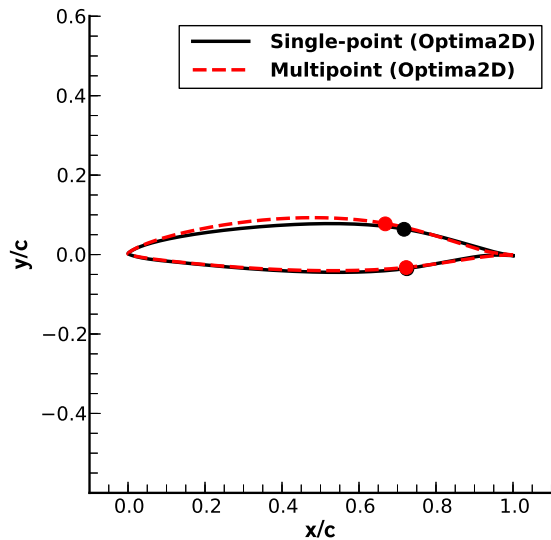
Table 7 provides a summary of the results comparing the initial and optimized airfoils, along with the various angles of attack. Note that the lift constraint has been satisfied and the drag reduced at each operating point. Note that the flight conditions and lift constraint of design point 6 correspond to the Case B single-point optimization presented in Section V.E. Figure 7(a) compares the single-point and multipoint optimized geometries for design point 6, and Fig 7(b) compares the pressure distributions. Comparing the optimized designs, it is clear that the single and multipoint results differ. The multipoint optimization has a transition point on the upper surface that is approximately 5% further upstream when compared to the single-point optimization of Case B. Furthermore, while the total drag was reduced by 53% in the single-point optimization, it was reduced by 50% in the multipoint optimization. This illustrates that the added robustness in the design (now optimized over a range of conditions) incurs a penalty in the on-design performance. It also exemplifies the importance of the designer's role in carefully selecting and weighting the design points appropriately. For example, if the Q400 normally cruises at the high-speed Mach number of 0.60, then the designer might choose to place more importance on those operating points.

Table 6. Design points and weighting for multipoint optimization

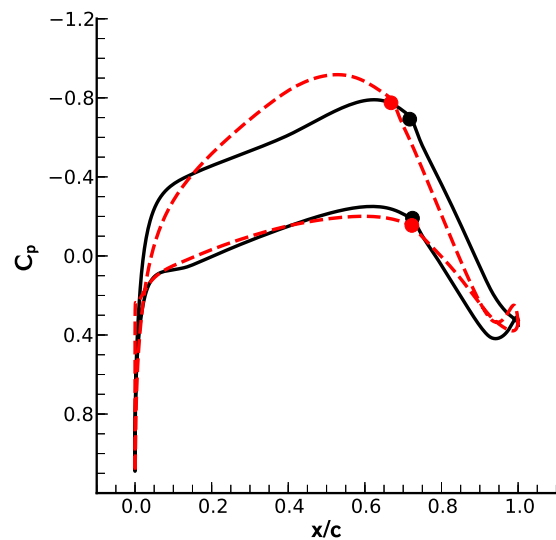
Design Pt.	Quadrature Weight ( $\mathcal{T}$ )	Aircraft Weight (W) [lbs]	Mach No. ( $M$ )	Reynolds No. ( $Re$ )	Lift Coefficient ( $C_l^*$ )
1	1	63757	0.48	$12.5 \times 10^6$	0.68
2	2	63757	0.54	$14.1 \times 10^6$	0.54
3	1	63757	0.60	$15.7 \times 10^6$	0.44
4	2	60754	0.48	$12.5 \times 10^6$	0.65
5	4	60754	0.54	$14.1 \times 10^6$	0.51
6	2	60754	0.60	$15.7 \times 10^6$	0.42
7	1	57751	0.48	$12.5 \times 10^6$	0.62
8	2	57751	0.54	$14.1 \times 10^6$	0.49
9	1	57751	0.60	$15.7 \times 10^6$	0.40

**Table 7. Summary of multipoint optimization results**

Design Pt.		$C_d$	$C_{d_p}$	$C_{d_v}$	$C_l$	$C_m$	$T_{up}(x/c)$	$T_{lo}(x/c)$	$AoA$
1	Initial	0.00803	0.00345	0.00458	0.6795	-0.07315	0.0172	0.5393	3.5050°
	Optimized	0.00453	0.00211	0.00241	0.6799	-0.08278	0.5509	0.7767	2.5651°
2	Initial	0.00692	0.00253	0.00439	0.5400	-0.07691	0.0620	0.5134	2.2177°
	Optimized	0.00328	0.00128	0.00200	0.5399	-0.08434	0.6656	0.7583	1.2498°
3	Initial	0.00613	0.00205	0.00408	0.4400	-0.08123	0.1328	0.4932	1.2852°
	Optimized	0.00304	0.00105	0.00199	0.4400	-0.08730	0.6664	0.7297	0.3184°
4	Initial	0.00778	0.00322	0.00458	0.6502	-0.07331	0.0199	0.5357	3.2765°
	Optimized	0.00393	0.00174	0.00219	0.6502	-0.08252	0.6194	0.7741	2.3059°
5	Initial	0.00670	0.00234	0.00436	0.5100	-0.07704	0.0763	0.5103	1.9920°
	Optimized	0.00318	0.00117	0.00200	0.5100	-0.08347	0.6685	0.7558	1.0383°
6	Initial	0.00598	0.00194	0.00405	0.4201	-0.08129	0.1479	0.4912	1.1430°
	Optimized	0.00300	0.00100	0.00200	0.4202	-0.08662	0.6683	0.7226	0.1875°
7	Initial	0.00761	0.00298	0.00463	0.6200	-0.07355	0.0232	0.5321	3.0357°
	Optimized	0.00368	0.00155	0.00213	0.6201	-0.08191	0.6421	0.7717	2.0713°
8	Initial	0.00656	0.00222	0.00434	0.4900	-0.07710	0.0860	0.5082	1.8419°
	Optimized	0.00311	0.00111	0.00200	0.4899	-0.08287	0.6705	0.7543	0.8963°
9	Initial	0.00584	0.00183	0.00401	0.4000	-0.08133	0.1634	0.4889	1.0000°
	Optimized	0.00301	0.00095	0.00206	0.4001	-0.08590	0.6701	0.6977	0.0527°



(a) Initial and optimized airfoils



(b) Point 6: Initial and optimized pressure distributions

**Figure 7. Comparison of single-point and multipoint optimization results (design point 6)**

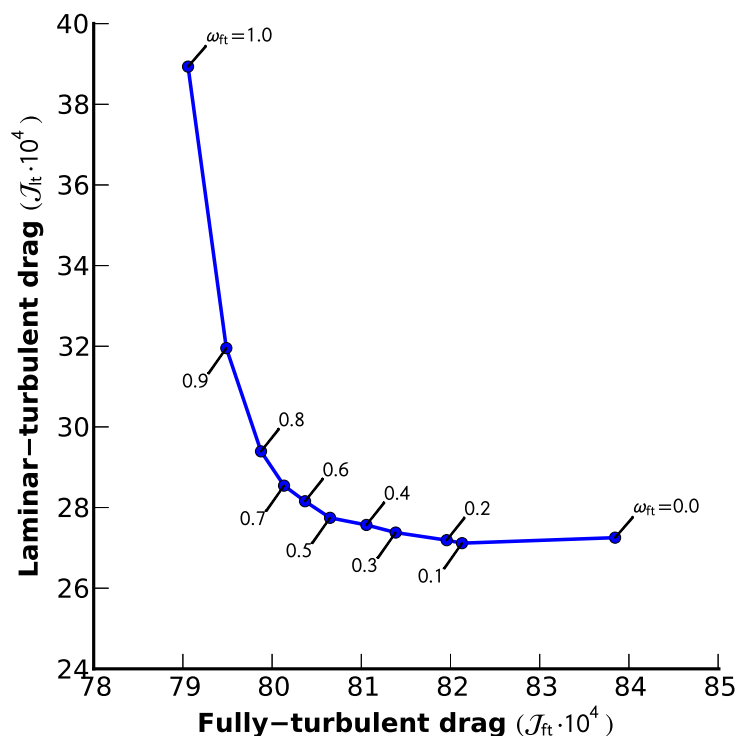


Figure 8. Pareto front study, Case B:  $Re = 15.7 \times 10^6$ ,  $M = 0.60$ ,  $C_l^* = 0.42$

## V.H. Case B: Pareto Front Study

A Pareto front can provide useful insight into the trade-offs involved in the design of NLF airfoils. While the multipoint optimization case (presented in Section V.G) is useful for designing an airfoil that performs well under perturbations about the cruise flight condition, here we consider the aerodynamic performance of NLF airfoils when or if transition occurs inadvertently at the leading edge of the airfoil.

Following the work of Driver and Zingg,<sup>21</sup> a Pareto front may be formed by minimizing a weighted sum objective,  $\mathcal{J}$ , defined as

$$\mathcal{J} = \omega_{ft} \mathcal{J}_{ft} + (1 - \omega_{ft}) \mathcal{J}_{lt}, \quad (19)$$

where  $\mathcal{J}_{ft}$  and  $\mathcal{J}_{lt}$  represent the drag coefficients under fully-turbulent and laminar-turbulent (i.e. free transition) conditions, respectively. Each point on the Pareto front represents a two-point design problem in which we minimize  $\mathcal{J}$  for a given weighting factor,  $\omega_{ft}$ , where  $0 \leq \omega_{ft} \leq 1$ . The calculation of the two operating conditions ( $\mathcal{J}_{ft}$  and  $\mathcal{J}_{lt}$ ) in turn requires two flow solutions, each at their respective angle of attack. Furthermore, both operating conditions are constrained to meet the same lift-target (set to  $C_l^* = 0.42$  for Case B) to ensure sufficient lift generation at both operating conditions for every optimal point.

The computed Pareto front is shown in Figure 8 and clearly captures the advantages of favouring one operating condition over the other. As expected, the drag count values under laminar-turbulent conditions are significantly less than the fully-turbulent operating conditions. The Pareto front demonstrates that when an airfoil designed strictly for laminar-turbulent conditions (that is,  $\omega_{ft} = 0$ ) is operating under fully-turbulent conditions, it has a drag count of approximately 84, as compared to 79 counts for an airfoil designed and operated under fully-turbulent conditions ( $\omega_{ft} = 1$ ); a relative drag penalty of approximately 6%. On the other hand, when an airfoil designed strictly for fully-turbulent conditions is operating under laminar-turbulent conditions it has a drag count of approximately 39, as compared to 27 counts for an airfoil designed and operated under laminar-turbulent conditions; a relative drag penalty of approximately 44%. The remaining points on the Pareto front allow the designer to select an appropriate optimal geometry depending on their needs and conservatism. Airfoils optimized using  $\omega_{ft}$  values in the range of  $0.3 \leq \omega_{ft} \leq 0.7$  represent a good compromise in performance between the two operating conditions.

## VI. Conclusions

A two-dimensional RANS solver making use of the Spalart-Allmaras turbulence model has been extended to incorporate an iterative laminar-turbulent transition prediction methodology. With reasonable grid density, the boundary-layer properties can be computed directly from the Navier-Stokes solution with sufficient accuracy. The compressible form of the AHD criterion and the simplified  $e^N$  envelope method have been implemented, verified, and validated by comparison to numerical and experimental data.

The RANS solver was subsequently employed in a gradient-based sequential quadratic programming shape optimization framework using the SNOPT optimization suite. The gradients are evaluated using a new augmented discrete-adjoint formulation for transition prediction in a RANS solver, the accuracy of which has been verified. The resulting optimization framework has been applied to the design of natural-laminar-flow airfoils using single and multipoint optimizations, as well as a Pareto front study. Such applications demonstrate the efficacy and practicality of using high-fidelity aerodynamic shape optimization as an NLF design tool in the subsonic and transonic flight regime. Future work will consider the extension of the current methodology to three dimensions, incorporating a crossflow transition criterion.

## VII. Acknowledgements

The authors gratefully acknowledge the financial assistance of the Ontario Government, Mathematics of Information Technology and Complex Systems, Canada Research Chairs Program, Bombardier Aerospace, and the University of Toronto.

## References

- <sup>1</sup>Marburger, J. H., "National Aeronautics Research and Development Plan," Technical report, National Science and Technology Council, February 2010.
- <sup>2</sup>White, F. M., *Viscous Fluid Flow*, McGraw-Hill, Inc., 3rd ed., 2005.
- <sup>3</sup>Fujino, M., Yoshizaki, Y., and Kawamura, Y., "Natural-Laminar-Flow Airfoil Development for a Lightweight Business Jet," *Journal of Aircraft*, Vol. 40, No. 4, July 2003, pp. 609–615.
- <sup>4</sup>Campbell, R., Campbell, M., and Streit, T., "Progress Toward Efficient Laminar Flow Analysis and Design," *29th AIAA Applied Aerodynamics Conference*, No. AIAA-2011-3527, American Institute of Aeronautics and Astronautics, Jun 2011.
- <sup>5</sup>Sturdza, P., *An Aerodynamic Design Method for Supersonic Natural Laminar Flow Aircraft*, Ph.D. thesis, Stanford University, December 2003.
- <sup>6</sup>Brodeur, R. R. and van Dam, C. P., "Transition Prediction for a Two-Dimensional Reynolds-averaged Navier-Stokes Method Applied to Wind Turbine Airfoils," *Wind Energy*, Vol. 4, No. 2, October 2001, pp. 61–75.
- <sup>7</sup>Zingg, D. and Godin, P., "A perspective on turbulence models for aerodynamic flows," *International Journal of Computational Fluid Dynamics*, Vol. 23, No. 4, April 2009, pp. 327–335.
- <sup>8</sup>Reed, H. L. and Saric, W. S., "Transition Mechanisms for Transport Aircraft," *38th Fluid Dynamics Conference and Exhibit*, No. AIAA-2008-3743, Seattle, Washington, June 2008.
- <sup>9</sup>Arnal, D., Casalis, G., and Houdeville, R., "Practical Transition Prediction Methods: Subsonic and Transonic Flows," *VKI Lecture Series: Advances in Laminar-Turbulent Transition Modeling*, January 2009.
- <sup>10</sup>Krimmelbein, N., Nebel, C., and Radespiel, R., "Numerical Aspects of Transition Prediction for Three-Dimensional Configurations," *35th AIAA Fluid Dynamics Conference & Exhibit*, No. AIAA-2005-4764, Toronto, Ontario, June 2005.
- <sup>11</sup>Krumbein, A., " $e^N$  transition prediction for 3D wing configurations using database methods and a local, linear stability code," *Aerospace Science and Technology*, Vol. 12, No. 8, December 2008, pp. 592–598.
- <sup>12</sup>Stock, H. W. and Haase, W., "Navier-Stokes Airfoil Computations with  $e^N$  Transition Prediction Including Transitional Flow Regions," *AIAA Journal*, Vol. 38, No. 11, November 2000, pp. 2059–2066.
- <sup>13</sup>Stock, H. W. and Seitz, A., "Crossflow-Induced Transition Prediction Using Coupled Navier-Stokes and  $e^N$  Method Computations," *AIAA Journal*, Vol. 42, No. 9, September 2004, pp. 1746–1754.
- <sup>14</sup>Nebel, C., Radespiel, R., and Wolf, T., "Transition Prediction for 3D Flows Using a Reynolds-Averaged Navier-Stokes Code and N-Factor Methods," *33rd AIAA Fluid Dynamics Conference and Exhibit*, Jun 2003.
- <sup>15</sup>Moens, F., Perraud, J., Krumbein, A., Toulorge, T., Iannelli, P., P., E., and Hanifi, A., "Transition prediction and impact on a three-dimensional high-lift-wing configuration," *Journal of Aircraft*, Vol. 45, No. 5, September 2008, pp. 1751–1766.
- <sup>16</sup>Streit, T., Horstmann, H., Shraut, G., Hein, S., Fey, U., Egmai, Y., Perraud, J., Salah El Din, I., Cella, U., and Quest, J., "Complementary Numerical and Experimental Data Analysis of the ETW Telfona Pathfinder Wing Transition Tests," *49th Aerospace Sciences Meeting and Exhibit*, No. AIAA-2011-881, Orlando, Florida, January 2011.
- <sup>17</sup>Mayda, E., *Boundary Layer Transition Prediction for Reynolds-Averaged Navier-Stokes Methods*, Ph.D. thesis, University of California, Davis, 2007.
- <sup>18</sup>Cliquet, J., Houdeville, R., and Arnal, D., "Application of Laminar-Turbulent Transition Criteria in Navier-Stokes Computations," *AIAA Journal*, Vol. 46, No. 5, May 2008, pp. 1182–1190.
- <sup>19</sup>Cebeci, T. and Cousteix, J., *Modeling and Computation of Boundary-Layer Flows*, Springer, Long Beach, 2nd ed., 2005.

- <sup>20</sup>Krumbein, A., "On Modeling of Transitional Flow and its Application on a High Lift Multi-Element Airfoil Configuration," *41st Aerospace Sciences Meeting and Exhibit*, No. AIAA-2003-724, Reno, Nevada, January 2003.
- <sup>21</sup>Driver, J. and Zingg, D. W., "Numerical Aerodynamic Optimization Incorporating Laminar-Turbulent Transition Prediction," *AIAA Journal*, Vol. 45, No. 8, August 2007, pp. 1810-1818.
- <sup>22</sup>Langtry, R. B. and Menter, F. R., "Transition Modeling for General CFD Applications in Aeronautics," *43rd AIAA Aerospace Sciences Meeting and Exhibit*, No. AIAA-2005-522, Reno, Nevada, 10-13 January 2005.
- <sup>23</sup>Langtry, R. B. and Menter, F. R., "Correlation-Based Transition Modeling for Unstructured Parallelized Computational Fluid Dynamics Codes," *AIAA Journal*, Vol. 47, No. 12, December 2009, pp. 2894-2906.
- <sup>24</sup>Medida, S. and Baeder, J. D., "Application of the Correlation based  $\gamma-Re_{\theta_t}$  Transition Model to the Spalart-Allmaras Turbulence Model," *20th AIAA Computational Fluid Dynamics Conference*, No. AIAA-2011-3979, Honolulu, Hawaii, June 2011.
- <sup>25</sup>Aranake, A., Lakshminarayan, V., and Duraisamy, K., "Assessment of Transition Model and CFD Methodology for Wind Turbine Flows," *42nd AIAA Fluid Dynamics Conference and Exhibit*, No. AIAA-2012-2720, June 2012.
- <sup>26</sup>Coder, J. and Maughmer, M., "A CFD-Compatible Transition Model Using an Amplification Factor Transport Equation," *51st AIAA Aerospace Sciences Meeting including the New Horizons Forum and Aerospace Exposition*, Jan 2013.
- <sup>27</sup>Rashad, R. and Zingg, D. W., "Toward High-Fidelity Aerodynamic Shape Optimization for Natural Laminar Flow," *21st AIAA Computational Fluid Dynamics Conference*, No. AIAA-2013-2583, San Diego, CA, June 2013.
- <sup>28</sup>Drela, M. and Giles, M. B., "Viscous-inviscid analysis of transonic and low Reynolds number airfoils," *AIAA Journal*, Vol. 25, No. 10, Oct 1987, pp. 1347-1355.
- <sup>29</sup>Krimmelbein, N. and Radespiel, R., "Transition prediction for three-dimensional flows using parallel computation," *Computers & Fluids*, Vol. 38, No. 1, 2009, pp. 121-136.
- <sup>30</sup>Kroo, I. and Sturdza, P., "Design-Oriented Aerodynamic Analysis for Supersonic Laminar Flow Wings," *41st AIAA Aerospace Sciences Meeting & Exhibit*, No. AIAA-2003-0774, Reno, Nevada, 6-9 January 2003.
- <sup>31</sup>Sturdza, P., "Extensive Supersonic Natural Laminar Flow on the Aerion Business Jet," *45th AIAA Aerospace Sciences Meeting and Exhibit*, No. AIAA-2007-685, Desktop Aeronautics Inc., Reno, NV, January 2007.
- <sup>32</sup>Dodbele, S. S., "Design optimization of natural laminar flow bodies in compressible flow," *Journal of Aircraft*, Vol. 29, No. 3, May 1992, pp. 343-347.
- <sup>33</sup>Green, B. E., Whitesides, J. L., Campbell, R. L., and Mineck, R. E., "A Method for the Constrained Design of Natural Laminar Flow Airfoils," *14th AIAA Applied Aerodynamics Conference*, No. AIAA-96-2502, June 1996.
- <sup>34</sup>Pralits, J., *Optimal Design of Natural and Hybrid Laminar Flow Control on Wings*, Ph.D. thesis, Royal Institute of Technology Department of Mechanics, Stockholm, Sweden, October 2003.
- <sup>35</sup>Amoignon, O., Berggren, M., Hanifi, A., Henningson, D., and Pralits, J., "Shape Optimization for Delay of Laminar-Turbulent Transition," *AIAA Journal*, Vol. 44, May 2006, pp. 1009-1024.
- <sup>36</sup>Cameron, L., Early, J., and McRoberts, R., "Metamodel Assisted Multi-Objective Global Optimisation of Natural Laminar Flow Aerofoils," *29th AIAA Applied Aerodynamics Conference*, No. AIAA-2011-3001, Honolulu, Hawaii, June 2011.
- <sup>37</sup>Xu, J. and Kroo, I., "Aircraft Design with Active Load Alleviation and Natural Laminar Flow," *53rd AIAA/ASME/ASCE/AHS/ASC Structures, Structural Dynamics and Materials Conference*, No. 2012-1428, American Institute of Aeronautics and Astronautics, Honolulu, Hawaii, Apr 2012.
- <sup>38</sup>Lee, J. and Jameson, A., "Natural-Laminar-Flow Airfoil and Wing Design by Adjoint Method and Automatic Transition Prediction," *47th AIAA Aerospace Sciences Meeting and Exhibit*, No. AIAA-2009-897, Orlando, Florida, 5-8 January 2009.
- <sup>39</sup>Khayat-zadeh, P. and Nadarajah, S. K., "Aerodynamic Shape Optimization of Natural Laminar Flow (NLF) Airfoils," *50th AIAA Aerospace Sciences Meeting*, No. AIAA-2012-0061, Nashville, Tennessee, 9-12 January 2012.
- <sup>40</sup>Khayat-zadeh, P. and Nadarajah, S. K., "Laminar-turbulent flow simulation for wind turbine profiles using the  $\gamma-Re_{\theta_t}$  transition model," *Wind Energy*, Vol. 17, No. 6, 2013, pp. 901-918.
- <sup>41</sup>Zahle, F., Bak, C., Srensen, N. N., Vronsky, T., and Gaudern, N., "Design of the LRP airfoil series using 2D CFD," *Journal of Physics: Conference Series*, Vol. 524, Jun 2014, pp. 012020.
- <sup>42</sup>Jing, L., Zhenghong, G., Jiagntao, H., and Ke, Z., "Robust design of NLF airfoils, Chin J Aeronaut (2013), <http://dx.doi.org/10.1016/j.cja.2013.02.007>," *Chinese Journal of Aeronautics*, Vol. 26, No. 2, April 2013, pp. 309-318.
- <sup>43</sup>Zhao, K., Gao, Z.-h., and Huang, J.-t., "Robust design of natural laminar flow supercritical airfoil by multi-objective evolution method," *Appl. Math. Mech.-Engl. Ed.*, Vol. 35, No. 2, Jan 2014, pp. 191202.
- <sup>44</sup>Robitaille, M., *Conception aérodynamique d'un profil d'aile transsonique laminaire adaptable aux conditions de vol*, Master's thesis, École Polytechnique de Montréal, 2014.
- <sup>45</sup>Wang, X., Cai, J., Liu, C., and Hu, Z., "Airfoil Optimization Based on Rapid Transition Prediction," *56th AIAA/ASCE/AHS/ASC Structures, Structural Dynamics, and Materials Conference*, Jan 2015.
- <sup>46</sup>Buckley, H. P. and Zingg, D. W., "An Approach to Aerodynamic Design through Numerical Optimization," *AIAA Journal*, Vol. 51, No. 8, August 2013, pp. 1972-1981.
- <sup>47</sup>Khayat-zadeh, P. and Nadarajah, S. K., "Aerodynamic Shape Optimization via Discrete Viscous Adjoint Equations for the  $k-\omega$  SST Turbulence and  $\gamma-Re_{\theta}$  Transition Models," *49th AIAA Aerospace Sciences Meeting*, No. AIAA-2011-1247, Orlando, Florida, 4-7 January 2011.
- <sup>48</sup>Nemec, M. and Zingg, D. W., "Newton-Krylov Algorithm for Aerodynamic Design Using the Navier-Stokes Equations," *AIAA Journal*, Vol. 40, No. 6, June 2002, pp. 1146-1154.
- <sup>49</sup>Nemec, M., Zingg, D. W., and Pulliam, T. H., "Multipoint and Multi-Objective Aerodynamic Shape Optimization," *AIAA Journal*, Vol. 42, No. 6, June 2004, pp. 1057-1065.
- <sup>50</sup>Jameson, A., Schmidt, W., and Turkel, E., "Numerical solution of the Euler equations by finite volume methods using Runge-Kutta time-stepping schemes," *14th AIAA Fluid and Plasma Dynamics Conference*, No. AIAA-81-1259, Palo Alto, California, June 1981.

- <sup>51</sup>Swanson, R. and Turkel, E., “On central-difference and upwind schemes,” *Journal of Computational Physics*, Vol. 101, No. 2, Aug 1992, pp. 292–306.
- <sup>52</sup>Spalart, P. and Allmaras, S., “A One-Equation Turbulence Model for Aerodynamic Flows,” *30th AIAA Aerospace Sciences Meeting & Exhibit*, No. AIAA-092-0439, Reno, NV, January 1992.
- <sup>53</sup>Arnal, D., Houdeville, R., Seraudie, A., and Vermeersh, O., “Overview of laminar- turbulent transition investigations at ONERA Toulouse,” *41st AIAA Fluid Dynamics Conference and Exhibit*, No. AIAA-2011-3074, Honolulu, Hawaii, June 2011.
- <sup>54</sup>Krumbein, A., “Automatic Transition Prediction and Application to High-Lift Multi-Element Configurations,” *Journal of Aircraft*, Vol. 42, No. 5, 2005, pp. 1150–1164.
- <sup>55</sup>Gill, P. E., Murray, W., and Saunders, M. A., “SNOPT: An SQP Algorithm for Large-Scale Constrained Optimization,” *SIAM Review*, Vol. 47, No. 1, Jan 2005, pp. 99–131.
- <sup>56</sup>Nocedal, J. and Wright, S. J., *Numerical Optimization*, Springer, 2nd ed., 2006.
- <sup>57</sup>Squire, W. and Trapp, G., “Using Complex Variables to Estimate Derivatives of Real Functions,” *SIAM Review*, Vol. 40, No. 1, January 1998, pp. 110–112.
- <sup>58</sup>Martins, J. R. R. A., Sturdza, P., and Alonso, J. J., “The Connection Between the Complex-Step Derivative Approximation and Algorithmic Differentiation,” *39th Aerospace Sciences Meeting and Exhibit*, No. AIAA-2001-0921, Reno, NV, January 2001.
- <sup>59</sup>Buckley, H., Zhou, B. Y., and Zingg, D. W., “Airfoil Optimization Using Practical Aerodynamic Design Requirements,” *Journal of Aircraft*, Vol. 47, No. 5, September 2010, pp. 1707–1719.
- <sup>60</sup>Somers, D. M., “Design and Experimental Results for a Natural-Laminar-Flow Airfoil for General Aviation Applications,” Technical Paper 1861, National Aeronautics and Space Administration, June 1981.

## Appendix: Details of Transition Criteria

In the compressible form of the AHD criterion, outlined in Section III.A, the functions  $A$  through  $F$  are computed as a function of the Mach number at the boundary-layer edge,  $M_e$ , as follows:<sup>53</sup>

$$\begin{aligned}
 A &= 98.64M_e^3 - 356.44M_e^2 + 117.13M_e - 236.69 \\
 B &= -13.04M_e^4 + 38.5M_e^3 - 30.07M_e^2 + 10.89M_e + 22.7 \\
 C &= 0.21M_e^3 + 4.79M_e^2 - 1.76M_e + 22.56 \\
 D &= -3.48M_e^4 + 6.26M_e^3 - 3.45M_e^2 + 0.23M_e + 12 \\
 E &= 0.6711M_e^3 - 0.7379M_e^2 + 0.167M_e + 51.904 \\
 F &= 0.3016M_e^5 - 0.7061M_e^4 + 0.3232M_e^3 - 0.0083M_e^2 - 0.1745M_e + 14.6
 \end{aligned}$$

In the simplified  $e^N$  envelope method, outlined in Section III.B, the functions  $\frac{dN}{dRe_\theta}$ ,  $m$ , and  $l$  are given as follows:<sup>28</sup>

$$\begin{aligned}
 \frac{dN}{dRe_\theta} &= 0.01 \sqrt{[2.4H_k - 3.7 + 2.5 \tanh(1.5H_k - 4.65)]^2 + 0.25} \\
 m(H_k) &= \left( 0.058 \frac{(H_k - 4)^2}{H_k - 1} - 0.068 \right) \frac{1}{l(H_k)} \\
 l(H_k) &= \frac{6.54H_k - 14.07}{H_k^2}
 \end{aligned}$$